Positive- and Negative-Sequence Current Controller With Direct Discrete-Time Pole Placement for Grid-Tied Converters With LCL Filter

Diego Pérez-Estévez, *Student Member, IEEE*, Jesús Doval-Gandoy, *Member, IEEE*, Alejandro G. Yepes, *Member, IEEE*, and Óscar López, *Senior Member, IEEE*

***Abstract*—Traditionally, the current control of grid-tied converters with *LCL* filter is based on proportional-resonant or proportional-integral controllers, which often need an additional active damping method to achieve stability. These solutions do not permit to place the closed-loop poles in convenient locations when dealing with such high-order plants. This constraint results in degraded reference-tracking and disturbance-rejection responses. On the other hand, the existing methods based on direct pole placement or other modern control strategies, do not control with zero steady-state error both positive and negative sequences of the grid current, but only the positive one. This limitation is undesirable under unbalanced grid conditions. This paper presents a current controller for grid-tied converters with *LCL* filters based on direct discrete-time pole placement. The proposed controller makes it possible to control both positive and negative sequences of the grid-side current with zero steady-state error. Contrarily to the classical resonant controllers, the closed-loop poles can be placed in convenient locations, yielding a fast response with negligible overshoot and low controller effort. Moreover, no additional damping methods of the resonance are necessary to achieve stable operation, regardless of the switching frequency and *LCL* filter used. Simulation and experimental results that validate the proposal are presented.**

***Index Terms*—Grid-connected converter, *LCL* filter, parameter sensitivity, state-space current control.**

I. Introduction

GRID-CONNECTED converters are becoming more popular nowadays due to the increasing role of renewable energy sources and distributed power generation systems [1]. The voltage source converter (VSC) is one of the most common converter topologies used in this type of applications. In order to connect the two low-impedance voltage sources (the grid and the VSC), this solution needs a filter to attenuate the high-frequency currents generated by the VSC. Although different filter topologies can be considered, the *LCL* filter is the preferred option as a consequence of its reduced size and good performance [2] (it attenuates the grid-side current with a slope of 60 dB per decade above the resonant frequency). Nevertheless, the *LCL* filter presents a challenging problem to the designer of the current controller, because of its relatively high order and the small damping of its resonant poles [3].

A crucial part in a grid-tied converter is the current controller. Several current control strategies can be adopted. On the one hand, there are classical techniques such as proportional-integral control in one frame [4], in a double synchronous frame [5], and proportional resonant [6] controllers. Some of the classical methods, such as [5] and [4], are able to control both the positive and negative sequences. Nonetheless, they offer limited performance, because they do not permit to arbitrarily place the poles of the closed-loop system when dealing with a high-order plant such as that corresponding to the *LCL* filter plus the computational and modulation delay (one and a half samples, respectively [7]). This results in degraded reference-tracking and disturbance-rejection responses or even instability. Parker *et al.* [8] have analyzed the stability problem that arises when poles fall outside the unit circle, and determined that there is a threshold in the resonant frequency of the *LCL* filter: $f_s/6$. This critical frequency value determines the region where an additional damping strategy is necessary to make the system stable when controlling the grid-side current. The damping of the *LCL* filter can be implemented passively or actively. Although passive damping is the most commonly used method [9], it causes extra losses and reduces the efficiency of the system [10]. Active damping strategies overcome this problem. They usually rely on feeding back a signal obtained by filtering the capacitor current [11]–[14], the capacitor voltage [15]–[18], or the grid-side current [19]–[21]. Therefore, additional sensors or estimation mechanisms (e.g., deriving the capacitor voltage to obtain the capacitor current [15]) are needed. Furthermore, estimation mechanisms such as the derivative filtering usually present sensitivity problems to noise [15]. In addition, although active damping techniques move the closed-loop poles to stable regions [11]–[21], they still do not offer the freedom of placing the poles in a good location in terms of transient response, controller effort, and robustness to disturbances and parameter variations.

On the other hand, the modern control theory offers different methods such as linear quadratic (LQ) control [22], optimal control [23], model predictive control [24], [25], including

Manuscript received March 29, 2016; revised June 17, 2016 and September 5, 2016; accepted October 21, 2016. Date of publication October 26, 2016; date of current version April 24, 2017. This work was supported in part by the Spanish Ministry of Science and Innovation, in part by the European Commission, in part by the European Regional Development Fund under project DPI2016-75832, and in part by the FPU scholarship FPU14/00683. Recommended for publication by Associate Editor M. Liserre.

The authors are with the Applied Power Electronics Technology Group, University of Vigo, Vigo 36310, Spain (e-mail: dieperez@uvigo.es; jdoval@uvigo.es; agyepes@uvigo.es; olopez@uvigo.es).

Color versions of one or more of the figures in this paper are available online at http://ieeexplore.ieee.org.

Digital Object Identifier 10.1109/TPEL.2016.2621754

dead-beat control [26], [27], adaptive control [28], and direct pole placement (i.e., state feedback, which utilizes a compensator and an observer) [29]–[35]. These techniques already account for the damping of the open-loop poles of the plant, making it unnecessary to add more degrees of freedom or extra feedback branches to the controller to achieve a stable response.

Nevertheless, the solutions based on LQ or optimal control require a laborious selection of parameters that depend on the particular *LCL* filter and switching frequency used. Furthermore, in [22] and [23], there is not a direct relation between the design process and the performance obtained in the real system, in terms of controller effort and transient response. The ones based on pole placement are able to avoid these inconvenients. However, the previously proposed methods based on state-space control (including both the direct pole placement and LQ ones) [22], [30]–[34] do not model the plant losses of the VSC, the filter, and the grid impedance. This simplification represents the least damped scenario for the resonance of the *LCL* filter [32]. However, if the state-feedback controller is designed with a plant model different from the real plant, the response of the real system worsens. Therefore, estimated losses should be taken into account in the design of the controller in order to avoid a detriment of the performance. In addition, the designs in [22], [30]–[34] only control with zero steady-state error the positive sequence of the current, which makes the controller unsuitable for unbalanced grid conditions. In [29], a state-feedback controller is combined with an internal model controller to overcome this problem. Nevertheless, a detailed analysis for each particular *LCL* filter is needed, in order to evaluate the interactions that appear between both controllers. In [12], [26], [27], [29], and [35] robust controllers to grid impedance uncertainties are proposed; however, they are not tested under voltage sag faults. In case of sudden voltage dips, the dynamics of common grid-side current controllers, such as [12], [26], [27], [29], and [35], are normally too slow to prevent large current transients. Finally, the model predictive controllers in [24] and [25] offer a fast transient response; however, the switching frequency of the converter is variable because the switching states are directly selected by the control. This generates interharmonics in the grid-side current, which are hard to filter [24].

This paper presents a grid-side current controller for grid-tied converters with *LCL* filter that is able to control both positive and negative sequences of the fundamental grid frequency. The presented current controller uses the direct pole-placement strategy from the state-space theory. Contrarily to the classical controllers, the closed-loop poles are placed in convenient locations regardless of the *LCL*-filter resonant frequency and sampling frequency, and without adding an extra active damping method. Placing the poles in the specified locations results in a predictable and fast transient response, with low controller effort and no overshoot, and a good robustness to disturbances. Thus, a direct relation exists between the design process and the performance of the real system. Moreover, the reference-tracking and the disturbance-rejection capabilities, as well as the controller effort, do not depend on the *LCL*-filter resonance and sampling frequency used, when the design is performed according to the real values.

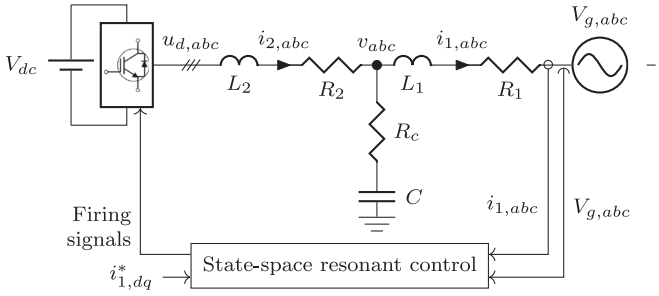

Fig. 1. Grid-tied VSC with *LCL* filter and grid-side current controller.

In addition, the controller structure used in this paper (state-command structure) provides a better response to reference tracking than the structure typically used with transfer function design (output-error-command structure), where the controller is placed in the direct path between the reference and the plant input. Furthermore, the controller also takes estimated plant losses into account, in order to avoid the detriment of the robustness and performance. The robustness of the control to parameter variations, including those of the grid impedance, is also evaluated, obtaining a low sensitivity.

After this introduction the remainder of this paper is organized as follows. Section II presents the models of the plant and the grid-voltage disturbance. In Section III, the compensator and the observer are designed, and the performance of the proposed current controller concerning its time response is analyzed. Then, in Section IV, its robustness is assessed by evaluating the sensitivity to model parameter variations and the disturbance-rejection capability. In Section V, simulation and experimental results that validate the theory are presented. Finally, conclusions are presented in Section VI.

II. Modeling of the Plant and the Disturbance

This section presents the models of the system dynamics (plant and disturbances) for the grid-side current controller shown in Fig. 1, where L_1, L_2, and C represent the reactive elements of the *LCL* filter; R_1, R_2, and R_c model the equivalent series resistances (ESRs) of the filter and the VSC [7]; $u_{d,\mathrm{abc}}$ is the VSC output voltage; $i_{1,\mathrm{abc}}$, $i_{2,\mathrm{abc}}$, and v_{abc} are the *LCL*-filter state variables (the converter-side current, the grid-side current, and the capacitor voltage, respectively); $V_{g,\mathrm{abc}}$ is the grid voltage; and $i^*_{1,dq}$ denotes the grid-side current reference in the direct quadrature (dq) frame. Since the grid-side current is controlled, the impedance that the VSC presents at the point of common coupling (PCC) can be arbitrarily specified. This permits working at unity power factor (generating a current reference with $i^*_q = 0$). In this manner, no reactive power exchange between the grid and the VSC is drawn during operation. The modeling process takes place in several steps throughout the section; each step adds features to the model obtained in the previous stage.

A. Model of the Plant for the Compensator

In the first place, a continuous model, including losses, of the *LCL* filter in stationary frame is presented. This model relates

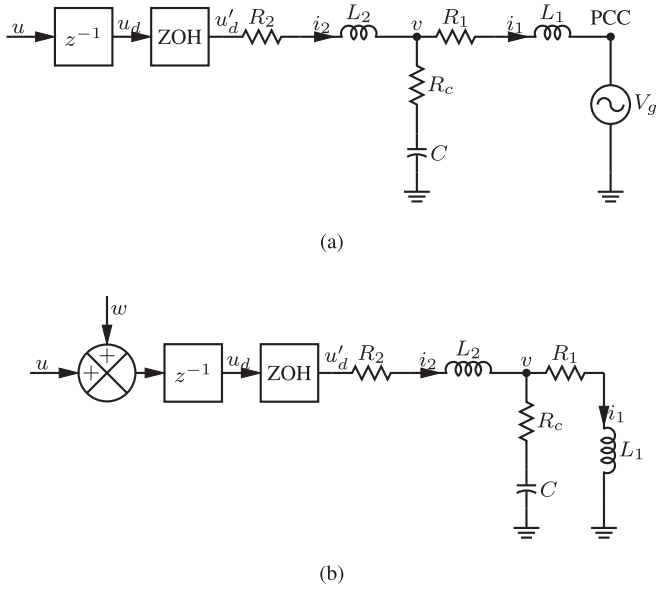

Fig. 2. Stationary-frame plant diagrams: *LCL* filter, PWM (modeled as a ZOH), and one-sample computational delay. (a) Real plant model: the grid voltage V_g is applied at the PCC. (b) Equivalent plant model: the grid voltage V_g is eliminated and an input equivalent disturbance w is defined.

the grid-side current $i_1(t)$ to the VSC output voltage $u'_d(t)$ for the *LCL* filter of the plant shown in Fig. 2(a) (the absence of reference frame in a subscript of a variable means $\alpha\beta$ frame). The first-order differential equations in the continuous domain (written in state-space form) are given as

$$\frac{d\mathbf{x}(t)}{dt} = \underbrace{\begin{bmatrix} \frac{-R_1}{L_1} & 0 & \frac{1}{L_1} \\ 0 & \frac{-R_2}{L_2} & \frac{-1}{L_2} \\ \frac{CR_cR_1 - L_1}{CL_1} & \frac{L_2 - CR_cR_2}{CL_2} & \frac{-(R_cL_1 + R_cL_2)}{L_1L_2} \end{bmatrix}}_{\mathbf{A}} \mathbf{x}(t) + \underbrace{\begin{bmatrix} 0 & \frac{1}{L_2} & \frac{R_c}{L_2} \end{bmatrix}^{\mathrm{T}}}_{\mathbf{B}} u'_d(t)$$

$$i_1(t) = \underbrace{\begin{bmatrix} 1 & 0 & 0 \end{bmatrix}}_{\mathbf{C}} \mathbf{x}(t)$$

$$\mathbf{x}(t) = \begin{bmatrix} i_1 & i_2 & v \end{bmatrix}^{\mathrm{T}}. \tag{1}$$

Boldface denotes a vector or a matrix. Equation (1) does not include the effect of the grid voltage V_g applied at the PCC in the state variables. This voltage disturbance is handled in a special way, using a disturbance estimation method [36], as explained later.

Next, (1) is discretized by using a zero-order-hold (ZOH) equivalent [36]. The sampling period T_s is equal to a switching period if a single-update strategy is used, and half the switching period in the case of a double-update strategy [37]. The pulse width modulator (PWM) with triangular carrier, when approximated as a ZOH, takes into account the half a sample delay added by the VSC PWM [7] (more accurate converter discretization methods for different carrier signals can be found in [38]–[40]). The resulting model relates the modulator voltage reference $u_d(k)$ with the sampled grid-side current $i_1(k)$

$$\begin{aligned} \mathbf{x}(k+1) &= \mathbf{F}\mathbf{x}(k) + \mathbf{G}u_d(k) \\ i_1(k) &= \mathbf{H}\mathbf{x}(k). \end{aligned} \tag{2}$$

Then, a one-sample input (computational) delay is added. The model of this delay on the modulator voltage $u(k)$ is given as [36]

$$u_d(k+1) = u(k). \tag{3}$$

In this manner, combining (2) and (3), the system model that takes the computational delay into account is given as

$$\underbrace{\begin{bmatrix} \mathbf{x}_1(k+1) \\ u_d(k+1) \end{bmatrix}}_{\mathbf{x}_2(k+1)} = \underbrace{\begin{bmatrix} \mathbf{F_1} & \mathbf{G_1} \\ \mathbf{0} & 0 \end{bmatrix}}_{\mathbf{F_2}} \underbrace{\begin{bmatrix} \mathbf{x}_1(k) \\ u_d(k) \end{bmatrix}}_{\mathbf{x}_2(k)} + \underbrace{\begin{bmatrix} \mathbf{0} \\ 1 \end{bmatrix}}_{\mathbf{G_2}} u(k)$$

$$i_1 = \underbrace{\begin{bmatrix} \mathbf{H_1} & 0 \end{bmatrix}}_{\mathbf{H_2}} \underbrace{\begin{bmatrix} \mathbf{x}_1(k) \\ u_d(k) \end{bmatrix}}_{\mathbf{x}_2(k)}$$

$$\mathbf{x}_2(k) = \begin{bmatrix} i_1 & i_2 & v & u_d \end{bmatrix}^{\mathrm{T}}. \tag{4}$$

The resultant model relates the grid-side current $i_1(k)$ to the modulator voltage $u(k)$ in the plant shown in Fig. 2(a). Equation (4) is the plant model to be controlled by the compensator.

B. Model of the Plant and the Disturbance for the Observer

In order to eliminate the steady-state error due to the grid voltage V_g (no feedforward of V_g is implemented) and plant modeling mismatches, the proposed controller includes a resonant action in the observer. The resonant action is obtained by placing two conjugated open-loop poles in the observer at the fundamental grid-voltage frequency ω_g (i.e., at position $z = e^{\pm j\omega_g T_s}$) so as to control both positive and negative sequences. There are two different possibilities for implementing the disturbance model in the control (in this case, the resonant action) by means of state-space methods: state augmentation and disturbance estimation [36]. The latter is chosen here for the reasons explained in Section III, and determines the way in which the plant and the disturbance should be modeled for the observer.

In the following, the model of the plant and the disturbance for the observer is developed. First, the grid voltage V_g is eliminated from the PCC and an input equivalent disturbance w is defined [36], as shown in Fig. 2(b). Next, a model of the disturbance w should be specified. A sinusoidal disturbance $w(t)$ of frequency ω_g, which contains both sequences (two complex conjugate poles in its model), is a solution of

$$\frac{d^2w(t)}{dt^2} = -\omega_g^2 w(t) \tag{5}$$

which, in matrix notation, corresponds to

$$\frac{d\mathbf{r}(t)}{dt} = \underbrace{\begin{bmatrix} 0 & 1 \\ -\omega_g^2 & 0 \end{bmatrix}}_{\mathbf{A_d}} \mathbf{r}(t)$$
$$w(t) = \underbrace{\begin{bmatrix} 1 & 0 \end{bmatrix}}_{\mathbf{C_d}} \mathbf{r}(t) \tag{6}$$

where

$$\mathbf{r}(t) = \begin{bmatrix} r_1 & r_2 \end{bmatrix}^{\mathrm{T}} = \begin{bmatrix} w & dw/dt \end{bmatrix}^{\mathrm{T}}. \tag{7}$$

Then, (6) is discretized by using a ZOH equivalent (again, to model the PWM effect), yielding the disturbance model

$$\mathbf{r}(k+1) = \mathbf{F_d}\mathbf{r}(k)$$
$$w(k) = \mathbf{H_d}\mathbf{r}(k). \tag{8}$$

In order to design an observer that estimates the input equivalent disturbance w [see Fig. 2(b)] at frequencies $\pm\omega_g$, the previous plant model (4) is augmented with the disturbance model (8) in order to include the resonant action:

$$\underbrace{\begin{bmatrix} \mathbf{x}_2(k+1) \\ \mathbf{r}(k+1) \end{bmatrix}}_{\mathbf{x}_3(k+1)} = \underbrace{\begin{bmatrix} \mathbf{F_2} & \mathbf{G_2}\mathbf{H_d} \\ \mathbf{0} & \mathbf{F_d} \end{bmatrix}}_{\mathbf{F_3}} \underbrace{\begin{bmatrix} \mathbf{x}_2(k) \\ \mathbf{r}(k) \end{bmatrix}}_{\mathbf{x}_3(k)} + \underbrace{\begin{bmatrix} \mathbf{G_2} \\ \mathbf{0} \end{bmatrix}}_{\mathbf{G_3}} u(k)$$
$$i_1(k) = \underbrace{\begin{bmatrix} \mathbf{H_2} & \mathbf{0} \end{bmatrix}}_{\mathbf{H_3}} \underbrace{\begin{bmatrix} \mathbf{x}_2(k) \\ \mathbf{r}(k) \end{bmatrix}}_{\mathbf{x}_3(k)}$$
$$\mathbf{x}_3(k) = \begin{bmatrix} i_1 & i_2 & v & u_d & r_1 & r_2 \end{bmatrix}^{\mathrm{T}}. \tag{9}$$

This is the model of the plant and disturbance that the observer uses to estimate the *LCL* state $\mathbf{x}_2$ and the input-equivalent grid-voltage disturbance w.

Notice that the sinusoidal disturbance w cannot be controlled; hence, it is not included in the model used by the compensator. Nevertheless, it does need to be known to be compensated; thus, it is included in the observer model [36].

III. Compensator and Observer Design using Pole Placement

Fig. 3 shows the proposed controller architecture. The caret on a variable name indicates that the variable is an estimate calculated by the observer, also named estimator [36]. The developed scheme only measures one state variable, the grid-side current[1] $i_{1,\mathrm{abc}}$. This state variable is transformed to the $\alpha\beta$ frame, the one where the controller is implemented, resulting in i_1. The inputs of the observer are the reference voltage after passing through the saturator u_{sat} and the measured grid-side current i_1. The input of the controller is the grid-side current reference i_1^*. The equation that the reduced-order observer implements is

[1]This can be accomplished with two current sensors, assuming no zero-sequence current is present.

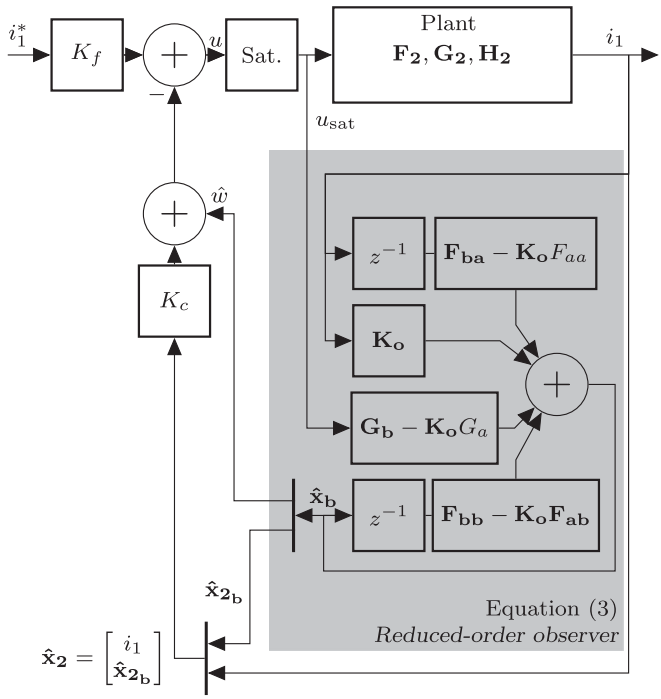

Fig. 3. Proposed controller architecture.

given as

$$\hat{\mathbf{x}}_\mathbf{b}(k) = (\mathbf{F_{bb}} - \mathbf{K_o}\mathbf{F_{ab}})\hat{\mathbf{x}}_\mathbf{b}(k-1) + \mathbf{K_o}i_1(k) + (\mathbf{F_{ba}} - \mathbf{K_o}F_{\mathrm{aa}})i_1(k-1) + (\mathbf{G_b} - \mathbf{K_o}G_a)u(k-1). \tag{10}$$

The constants F_{aa}, $\mathbf{F_{bb}}$, $\mathbf{F_{ab}}$, $\mathbf{F_{ba}}$, G_a, $\mathbf{G_b}$, and $\mathbf{K_o}$ used in (10) are given in the Appendix. Using the estimated state $\hat{\mathbf{x}}_\mathbf{b}(\mathbf{k})$ from (10), the modulator voltage in (3) is given as

$$u(k) = K_f i_1^* - \begin{bmatrix} \mathbf{K_c} & 1 & 0 \end{bmatrix} \begin{bmatrix} i_1 \\ \hat{\mathbf{x}}_\mathbf{b} \end{bmatrix}. \tag{11}$$

It should be noticed that $\mathbf{x}_\mathbf{b}^{\mathrm{T}} = \begin{bmatrix} x_{2b}^{\mathrm{T}} & r_1 & r_2 \end{bmatrix}$ includes the unmeasured states of the plant $x_{2b}^{\mathrm{T}} = [i_2 \;\; v \;\; u_d]$ and the disturbance estimation r_1 and r_2. In the implementation of the current controller from Fig. 3, the observer (10) uses $u_{\mathrm{sat}}(k-1)$ instead of $u(k-1)$. This gives a particularly simple antiwindup mechanism for this controller structure [41].

In order to obtain a fast response, the following two design choices are adopted: a state-command structure for the reference-input structure, and a disturbance-estimation structure for the resonant control. These two selections are explained in the following.

1) The state-command structure [36] is chosen because it presents a better response to situations related to reference tracking than that typically obtained with transfer-function design (output-error-command structure). The latter places the controller in the direct path between the reference and the plant input. On the other hand, the state-command structure, provides a direct path to the

plant (through the feedforward gain K_f and the saturator) for references to pass (see Fig. 3) and avoids exciting the controller modes. Thus, a faster response is obtained. This advantage is particularly worthy of note when high-order controllers, such as the proposed one, are used.

2) Among the two possibilities to implement the resonant action, state augmentation and disturbance estimation, the latter is adopted here. The first, state augmentation, adds the resonant action in the direct path from reference to plant input resulting in a slower response to reference changes because of the excited extra modes. In the case of the integral control, it is possible to place an additional zero that cancels the extra closed-loop pole introduced by the integrator [32]. However, this cancellation is never perfect due to plant uncertainties. The second possibility, disturbance estimation, implements the resonant action as part of the observer. Therefore, only disturbance rejection is affected by the extra two poles introduced by the resonant action.

The response to broadband signals like sags or reference current changes is determined by the bandwidth of the controller. High-bandwidth controllers allow fast signals (high frequencies) to pass in the case of references, or to be compensated in the case of disturbances. However, the speed at which the output can be controlled is limited to the available controller effort. The *LCL* filter attenuates signals above the resonant frequency ω_{res} with a slope of 60 dB per decade. Therefore, this low-pass behavior demands a huge effort from the controller when a high bandwidth is tried to be set. This fact results in the VSC entering into overmodulation. All types of current controllers have to cope with this fundamental limitation. The pole-placement strategy is designed in this section according to a radial projection [36] of the resonant poles of the plant so as to provide a good response while keeping the control effort low.

The compensator gain $\mathbf{K_c}$ and observer gain $\mathbf{K_o}$ (cf., Fig. 3), which determine the closed-loop poles of the system, are calculated according to the pole-placement strategy. MATLAB has two functions, `acker` and `place`, that can be used to calculate these two gains. Using direct discrete-time pole placement makes the design process straightforward compared with other state-space techniques such as LQ, where weighting matrices that are weakly connected to the performance specifications need to be specified [36]. In any case, it is necessary to define the position of the closed-loop poles. This is a crucial task that determines the performance of the control algorithm. In the following, the criteria developed to assign the closed-loop poles of the compensator and the observer are explained in detail. Note that the closed-loop poles of the complete system are the union of the compensator closed-loop poles and the observer closed-loop poles.

A. Radial Projection and Compensator Design

Radial projection (applied here to the resonant poles of the *LCL* filter) is a technique that minimizes control usage by simply adding damping to lightly damped open-loop poles without changing their frequency [36]. Thus, the proposed closed-loop

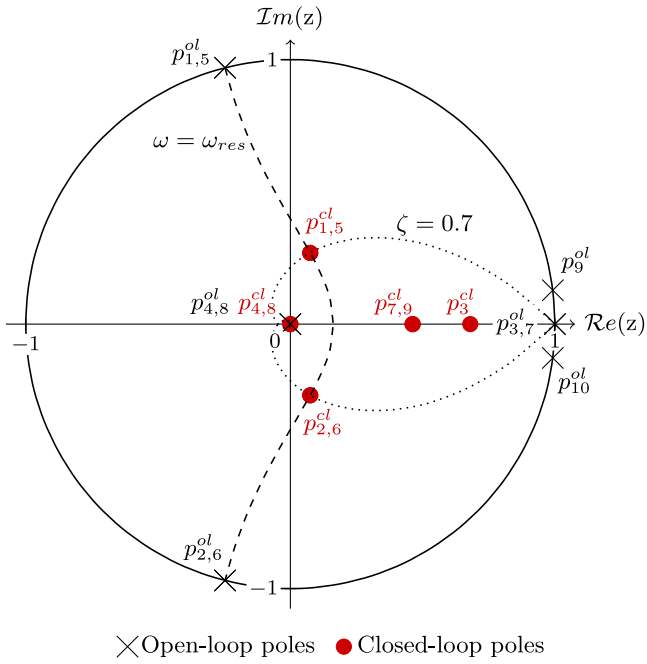

Fig. 4. Open- and closed-loop pole map of the complete system.

TABLE I
COMPENSATOR POLE PLACEMENT

	Position in the z-plane	
Poles	Open-loop	Closed-loop
	Radial projection of the *LCL* resonant poles to $\zeta = 0.7$.	
LCL filter	$p_{1,2}^{\text{ol}} = e^{\pm j\,\omega_{\text{res}} T_s}$	$p_{1,2}^{\text{cl}} = e^{-\zeta\,\omega_{\text{res}} \pm j\,\omega_{\text{res}} T_s \sqrt{1-\zeta^2}}$
	Moved to obtain higher bandwidth and to make it the dominant pole.	
	$p_3^{\text{ol}} = 1$	$p_3^{\text{cl}} = e^{-\omega_{\text{dom}} T_s}$
Comp. delay	Not moved; already in an optimum location.	
	$p_4^{\text{ol}} = 0$	$p_4^{\text{cl}} = 0$

location of the resonant poles is made dependent on the resonant frequency of the *LCL* filter so as to ensure uniform performance concerning the control effort regardless of the *LCL* filter used. Hence, a good response in combination with low controller effort are attained.

The plant model in (4) has four poles. The *LCL* filter has two complex conjugate poles $p_{1,2}^{\text{ol}}$ (the resonant poles) at the resonant frequency and a real pole p_3^{ol} at zero frequency. In addition, the computational delay adds a fourth pole p_4^{ol} to the model, at the origin of the z plane. These four poles are shown in Fig. 4, which depicts the pole map of the system.

In order not to unnecessarily increase the controller effort, the closed-loop poles should be kept close to the open-loop poles whenever the response is not significantly degraded [36]. Table I summarizes the proposed locations for the closed-loop poles of the compensator. The proposed current controller only reallocates three poles of the *LCL* filter ($p_{1,2,3}^{\text{ol}}$). One of them is displaced to a higher frequency (see p_3^{cl}, in Fig. 4); on the other

TABLE II
OBSERVER POLE PLACEMENT

Poles	Position in the z-plane: Open-loop	Position in the z-plane: Closed-loop
	Radial projection of resonant poles to $\zeta = 0.7$.	
LCL filter	$p_{5,6}^{\mathrm{ol}} = e^{\pm j\,\omega_{\mathrm{res}} T_s}$	$p_{5,6}^{\mathrm{cl}} = e^{-\zeta\,\omega_{\mathrm{res}} \pm j\,\omega_{\mathrm{res}} T_s\,\sqrt{1-\zeta^2}}$
	Moved to twice the frequency of the dominant pole.	
	$p_7^{\mathrm{ol}} = 1$	$p_7^{\mathrm{cl}} = e^{-2\omega_{\mathrm{dom}} T_s}$
Comp. delay	Not moved; already in an optimum location.	
	$p_8^{\mathrm{ol}} = 0$	$p_8^{\mathrm{cl}} = 0$
Resonant action	Moved to twice the frequency of the dominant pole.	
	$p_{9,10}^{\mathrm{ol}} = e^{\pm j\,\omega_g T_s}$	$p_9^{\mathrm{cl}} = e^{-2\omega_{\mathrm{dom}} T_s}$

hand, the other two are reallocated in a more damped region ($p_{1,2}^{\mathrm{cl}}$) to obtain a fast and damped response by means of radial projection (a damping factor ζ of 0.7 is used). The delay pole p_4^{ol} is already in an optimum location, so it is not moved. A frequency $f_{\mathrm{dom}} = \omega_{\mathrm{dom}}/2\pi = 150$ Hz is recommended for the dominant pole p_3^{cl}, because it ensures a negligible effect of the damped resonant poles $p_{1,2}^{\mathrm{cl}}$ on the system response (resonant frequencies above twice the dominant frequency, $f_{\mathrm{res}} > 300$ Hz, are expected). In this manner, contrarily to other current controllers, the response is not affected by the *LCL* filter choice. It should be noticed that the parameter f_{dom} can be modified to a value different from the recommended 150 Hz. However, further increasing the frequency of the dominant pole would demand more control effort to the VSC, because the magnitude of the transfer function that relates the grid-side current with the VSC output $G(s) = i_1/u$ rolls off at 20 dB per decade at frequencies below the resonant frequency [8].

Despite the fact that different *LCL* filters may have resonant poles in a wide frequency range (see $p_{1,2}^{\mathrm{ol}}$ in Table I), all *LCL* filters have a pole at zero frequency (see p_3^{ol} in Table I). Since this pole is moved and set to be the dominant pole of the system (see p_3^{cl} in Table I), the system bandwidth does not depend on the *LCL* filter used, but on this dominant closed-loop pole, and a consistent performance is obtained irrespectively of the filter installed.

B. Design of the Reduced-Order Observer

After the compensator closed-loop poles have been defined, the placement criteria of the observer closed-loop poles should be established. Table II summarizes the proposed location for the closed-loop poles of the observer. They are also shown in the pole map of the complete system in Fig. 4. Now the pole assignment is not restricted to yield a low control effort, because the observer does not drive any actuator, but simply calculates the state of the system. Therefore, a larger bandwidth can be set, and it is advisable to place the observer closed-loop poles ($p_{5,6,7,9}^{\mathrm{cl}}$) at frequencies higher (and damped) than that of the dominant pole of the compensator p_3^{cl} so as to provide similar dynamics to those of the compensator alone [36]. The computational delay pole p_8^{cl} is not moved because it is already in an optimum location.

Regarding the selection of the type of observer, there are three alternatives [36]: the predictor estimator, the current estimator, and the reduced-order estimator. Here, the reduced-order estimator is recommended because of the following reasons. The predictor estimator uses the next-to-last current measurement $i_1(k-1)$, instead of the last measurement $i_1(k)$, which gives a more recent state of the plant. The current estimator cannot be implemented in plants where there are pure delays, as the z^{-1} term of the computational delay. The reduced-order estimator eliminates one pole[2] (p_{10}^{ol}), making the response faster. This reduction in the order of the observer is of special convenience in order to obtain a fast disturbance rejection.

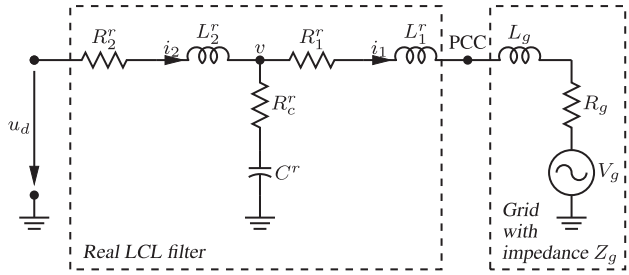

Fig. 5. Space-vector circuit model in $\alpha\beta$ coordinates of the real *LCL* filter, with values different from the nominal *LCL* filter of Fig. 2(a), connected to a grid with impedance $Z_g = R_g + j\omega L_g$.

IV. PARAMETER SENSITIVITY

A system that keeps a good regulation in the face of variations in the plant parameters is said to have low sensitivity to those parameters. In the case of a grid-tied inverter, there are several variables whose variation from the nominal value should be considered, namely, the grid impedance Z_g (which has an inductive part L_g and a resistive part R_g), the real *LCL* filter parameters (L_1^r, L_2^r, and C^r) [32], and the real ESR of the VSC [7] and of the *LCL* filter (R_1^r, R_2^r, and R_c^r).

A. Stability Regions

Since there are several degrees of freedom in the plant variation, a set of representative worst case scenario parameter values should be selected. This idea was also used in [32], where different stability regions were calculated for various real *LCL* filter parameters values that differ by a certain amount from the nominal value. In addition, an inductive grid, as in [32], is considered. The stability of the closed-loop system is analyzed by calculating the damping factor of the most unstable closed-loop pole (i.e., the smallest one) for each of the combinations of parameters considered. Now, the plant is modified from the ideal values (L_1, L_2, and C) of Fig. 2(a), used to design the controller, to the real values (L_1^r, $L_2^r + L_g$, and C^r), as shown in Fig. 5. The following three different cases are studied:

[2]The reduced-order estimator reduces its number of poles according to the number of state variables that are directly measured [36]. The proposed implementation only measures one state variable: the grid-side current i_1.

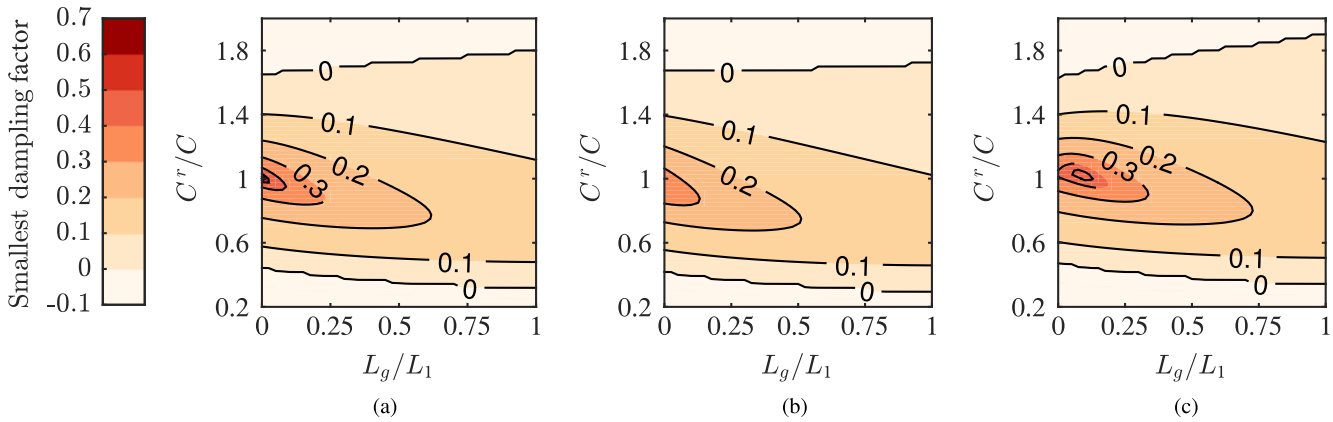

Fig. 6. Stability regions for variations in grid inductance L_g and the real *LCL*-filter capacitance C^r. (a) *LCL* filter-inductances with nominal values. (b) *LCL*-filter inductances with values 10% bigger than nominal. (c) *LCL*-filter inductances with values 10% smaller than nominal.

1) the filter inductances are the nominal ones: $L_1^r = L_1$ and $L_2^r = L_2$;

2) the filter inductances are 10% larger than the nominal values: $L_1^r = 1.1L_1$ and $L_2^r = 1.1L_2$;

3) the filter inductances are 10% smaller than the nominal ones: $L_1^r = 0.9L_1$ and $L_2^r = 0.9L_2$.

In all the cases, the real filter capacitance C^r is varied from $0.2C$ to $2C$ and the grid inductance L_g, from zero to L_1. Fig. 6 shows the resulting stability regions. It can be seen that the bigger the changes in the inductance or capacitance are, the smaller the damping factor of the least damped pole is. When the damping factor reaches zero, the system becomes unstable. For a 10% tolerance in the filter components, the analysis predicts a stable operation ($\zeta > 0$) in a wide range of situations. The system is specially robust to variations in the grid inductance L_g. Comparable results were obtained for the controller proposed in [32].

Selecting $L_1 = L_2$ a minimum cost of the total inductor $L_1 + L_2$ is obtained [2] (as done, e.g., in [2], [3], [13], [30], [34], [40]). Unmatched filter inductances could be considered [4] (e.g., $L_2 > L_1$ to reduce the rating of the switches for a required f_{res}) but a higher total inductor value would be obtained. From the control point of view, these changes do not have significant impact on the performance of the system because the position of the open-loop poles of the plant depends on the resultant resonant frequency, independently of the particular *LCL* filter values (L_1, C, and L_2) which give this resonant frequency.

B. Root Locus for L_g and ESRs Sweeps, and Pole Map for a Weak Grid

Any variation from the plant parameters used to design the controller will result in the closed-loop poles moving away from the desired location. The following analysis calculates the root locus of the closed-loop poles when certain parameters (L_g and the ESRs) are modified so as to evaluate the effect, as a whole, on all the closed-loop poles of the controller. Fig. 7 shows the root locus of the transfer function from the current reference i_1^* to the grid-side current i_1 in two cases: when the grid inductance is increased, and when the ESRs are not negligible but they are ignored in the controller design. It also shows the pole map of the system when the VSC is connected to a weak grid and the grid impedance is not included in the model used for the control design (the ESRs, for $r = 1$, are taken into account). The parameters of filter II from Table III are used for the analysis.

Fig. 7(a) shows a sweep in the grid inductance L_g from zero to a value equal to the *LCL*-filter grid-side inductance L_1. There are four poles that exhibit a greater sensitivity. As shown in the root locus, the sensitivity is not constant with parameter variation. Small initial variations cause big displacement in these four poles, whereas large additional parameter changes do not significantly worsen the response. However, the least damped poles are still the two complex conjugate poles associated with the resonance of the *LCL* filter; hence, they are still the ones that determine the stability.

Fig. 7(b) shows the effect of adding the ESRs of the filter components and the VSC ($R_1^r = rR_1$; $R_2^r = rR_2$; and $R_c^r = rR_c$ with $r \in [0, 1]$) for a controller designed without taking them into account, i.e., assuming $r = 0$, as in [32], and connected to an ideal grid ($Z_g = 0$). As it happens, any deviation from the nominal model moves the closed-loop poles from their desired location, degrading the control performance. Therefore, if estimated ESR values are available to the designer, it is recommended to take them into account. In any case, the variations in the ESRs only have a small effect on the transient response; thus, the proposed controller can be considered to be robust to them. Fig. 7(b) also shows the closed-loop poles when the VSC is connected to a weak grid. Now the grid impedance is the parameter that is not accounted for in the model, instead of the ESRs of the filter and the converter. The considered grid impedance $Z_g = 0.11$ per unit (p.u.) has a resistive part of 1.2 Ω, $R_g = 0.11$ p.u., and a reactive part of 330 μH, $L_g = 0.01$ p.u. (weak grids typically have a mainly resistive character [42]). This weak grid causes the closed-loop poles to move from the desired locations (worsening to a certain extent the response) when its impedance is not included in the plant model used to design the controller. Nevertheless, its effect (the pole movement) is small due to the robustness of the proposed controller.

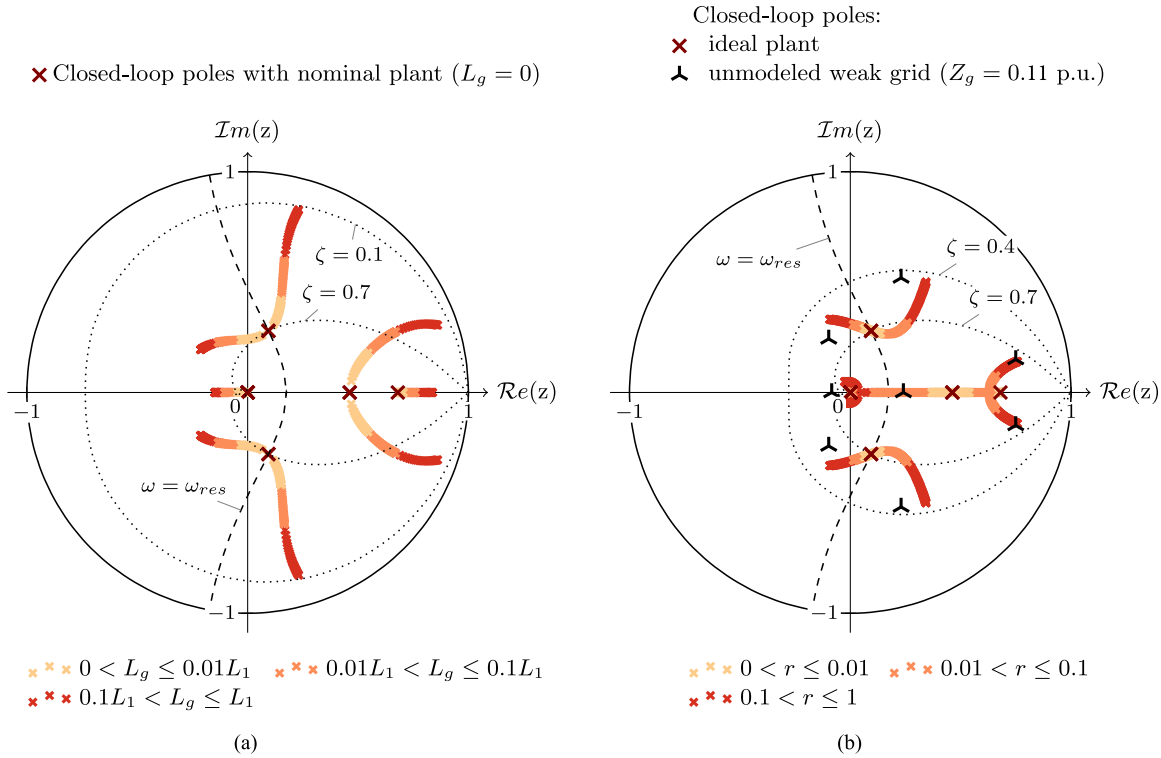

Fig. 7. Root locus of the complete system under different parameter variations. (a) Grid inductance L_g is increased from zero to a value equal to the *LCL*-filter grid-side inductance L_1. (b) Effect of adding the ESR of the filter components and the VSC for a controller designed with ideal plant parameters and operated with a plant with parameters $R_1^r = rR_1$, $R_2^r = rR_2$, and $R_c^r = rR_c$; and closed-loop poles when the VSC is connected to a weak grid of impedance $Z_g = 0.11$ per unit (p.u.) (the ESRs, for $r = 1$, are included in the model used to design the controller and the grid impedance Z_g is not included).

TABLE III
LCL FILTER PARAMETERS

Parameter	Filter I	Filter II*
L_1	2.7 mH	7.5 mH
L_2	2.7 mH	7.5 mH
C	30 μF	50 μF
R_1	0.25 Ω	0.5 Ω
R_2	0.5 Ω	0.75 Ω
R_c	0.1 Ω	0.1 Ω
f_{res}	791 Hz	367 Hz

*Filter II is not intended to be a high-performance filter design like filter I, but to validate the proposed current controller in a wide range of resonant frequencies of the *LCL* filter (below and above $f_s/6$).

V. EXPERIMENTAL RESULTS

The proposed current controller is tested in a 20-kW VSC working as an inverter and connected to a 400-V line-to-line 50-Hz three-phase grid (a three-phase ac voltage source was used to generate the voltage sags). The switching and sampling frequency is $f_s = 2.5$ kHz, with 3-μs dead-time. Since the single-update strategy represents the worst case control scenario, this one was chosen for the implementation. A double-update strategy executes the control algorithm at twice the speed of a single-update strategy [37]. Therefore, the computational delay is reduced. The dc-bus voltage is $v_{\text{dc}} = 750$ V. The two filters with different resonant frequencies f_{res} presented in Table III are used to connect the VSC to the grid. The design of filter I was carried out according to [4], obtaining a 1.4% of grid-side current ripple. Filter II was designed to validate the proposed current controller in a wide range of resonant frequencies of the *LCL* filter. Therefore, two different resonant frequencies for the *LCL* filter ($f_{\text{res},1} = 791$ Hz and $f_{\text{res},2} = 367$ Hz) are chosen (above and below $f_s/6 = 417$ Hz) in order to assess the stability and performance of the proposed controller in both stability regions established in [8]. If a higher sample rate were used, a resonant frequency below $f_s/6$ could also be obtained without increasing the value of the reactive elements. This would reduce the problems associated with high reactive values, such as higher losses, high voltage drop on the filter, and considerable reactive power drawing from the VSC. Unless otherwise stated, the *LCL* filter installed in each case corresponds to the filter parameters adopted for the design of the controller. Fig. 8(a) and (b) shows a diagram and a photograph of the experimental setup, respectively.

The following characteristics are tested with the controller being designed for each of the *LCL* filters: reference tracking of both sequences [see Figs. 9(a)–12(a) for *LCL* filter I, and Figs. 9(b)–12(b) for *LCL* filter II], disturbance rejection of both sequences see Figs. 13(a)–16(a) for *LCL* filter I, and Figs. 13(b)–16(b) for *LCL* filter II], disturbance rejection to voltage harmonics (see Fig. 17), and parameter sensitivity (see Figs. 18 and 19).

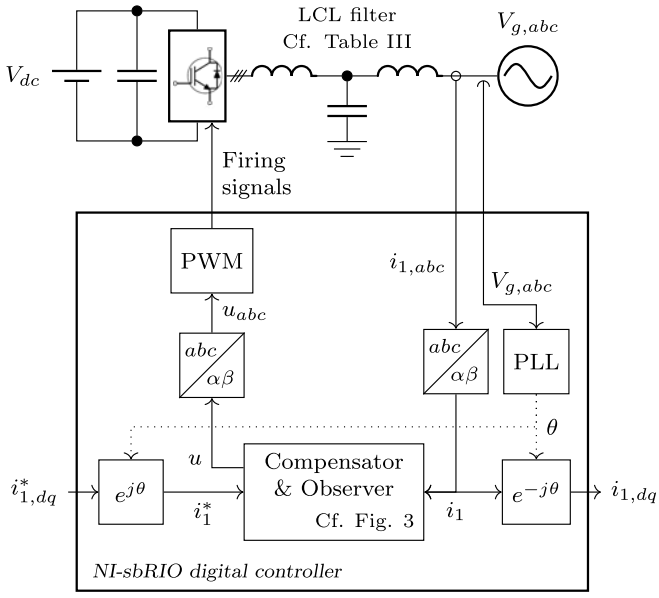

(a)

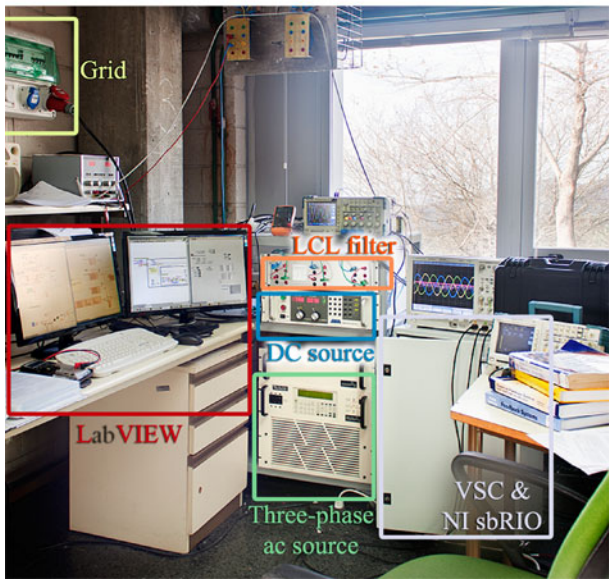

(b)

Fig. 8. Experimental setup. (a) Diagram. (b) Photograph.

Each test shows the reference signal i_1^*, the simulated response i_1^{sim}, and the measured response i_1. The simulated response accurately matches the experimental response in all the tests. The nonlinear effects of the VSC and the interaction between the current controller and the phase-loc ked loop (PLL) cause the negligible differences that can be observed between i_1 and i_1^{sim}. Although no phase jump is caused in the positive sequence of the grid voltage [43] and the PLL bandwidth is small, disturbances in the form of harmonics, noise, or transients present in the grid voltage can be introduced in the phase generated by the PLL [44].

Figs. 9 and 10 show a reference step in the q-axis of the positive-sequence dq frame (dq+ frame). The currents are also expressed in a synchronous frame rotating at the same frequency, so as to obtain a representation of characteristic parameters of dc signals (rise time, settling time, overshoot, and steady-state error) and the absence of cross coupling. The 10–90% rise time of the measured response i_1 in Fig. 9 is approximately 2.5 ms. This value is slightly greater than the rise time of a first-order system of the same bandwidth, $T_{10-90\%} = \ln|9|/(2\pi f_{\text{dom}}) = 2.33$ ms, due to the effect of the extra poles. Negligible overshoot is attained, as expected from the well-damped dominant closed-loop pole p_3^{cl} (see Fig. 4) placed at the frequency f_{dom}. The low-order harmonics (mainly sixth-order harmonic in the dq-frame) correspond to the fifth and seventh harmonics caused by nonlinearities of the VSC. Figs. 11 and 12 show an identical reference step, but now in the negative-sequence dq frame (dq− frame). The resulting response is of similar form to that obtained for the step in the other sequence (cf., Fig. 9), as intended, because the resonant action treats both sequences equally.

Figs. 13–19 display the robustness of the controller to both disturbances (e.g., sags and harmonics in the grid voltage) and parameter variations. Figs. 13 and 14 show the capability of the current controller to reject disturbances in the form of voltage sags (the sag contains both voltage sequences). A 40%-depth type-C sag [43] is generated with the three-phase ac-voltage source, while keeping the references constant. The settling time to within 2% is 6 ms, which is slightly greater than the $T_{\text{st}} = -\ln|0.02|/(2\pi f_{\text{dom}}) = 4.15$ ms associated with a first-order system, again due to the effect of the extra poles. The grid voltage at the instant when the voltage sag occurs has some high frequency oscillations [cf., Fig. 13(a)–16(a)] when the filter with lower impedance (filter I) is used. This is due to the limitation of the three-phase voltage source (model Pacific 360-AMX) to generate the defined voltage sag accurately at the PCC when connected to such a low impedance load (the VSC with filter I). This undesirable effect increases the settling time of the system. In order to see the response of the controller to reference changes during a sag condition, Figs. 15 and 16 show the reference-tracking capability under the same sag as in Fig. 13. The reference step i_1^* is calculated according the so-called positive-negative-sequence compensation strategy [45]. In this case, both currents, the grid-side current i_1 and its reference i_1^*, are shown in stationary frame because they both have a positive and a negative sequence simultaneously. The response is also fast and well damped when these effects (reference tracking and disturbance rejection of both sequences) are combined, as expected from the lineal model the system. The response may vary slightly depending on the initial phase of the sag, without altering the validity of such conclusion.

As anticipated, the rise time, the overshoot, and the settling time do not depend on the *LCL*-filter resonant frequency. This can be seen by comparing the oscilloscope captures obtained with filter I ($f_{\text{res}} < f_s/6$), shown in Figs. 9(a)–16(a), with those made with filter II ($f_{\text{res}} > f_s/6$), shown in Figs. 9(b)–16(b). This behavior results from the pole-placement criteria used in the design of the controller.

Fig. 17 shows the response to a reference step in the positive-sequence dq frame under the following conditions. The grid voltage has the following low-order voltage harmonics: $V_3 = 0.5\%$,

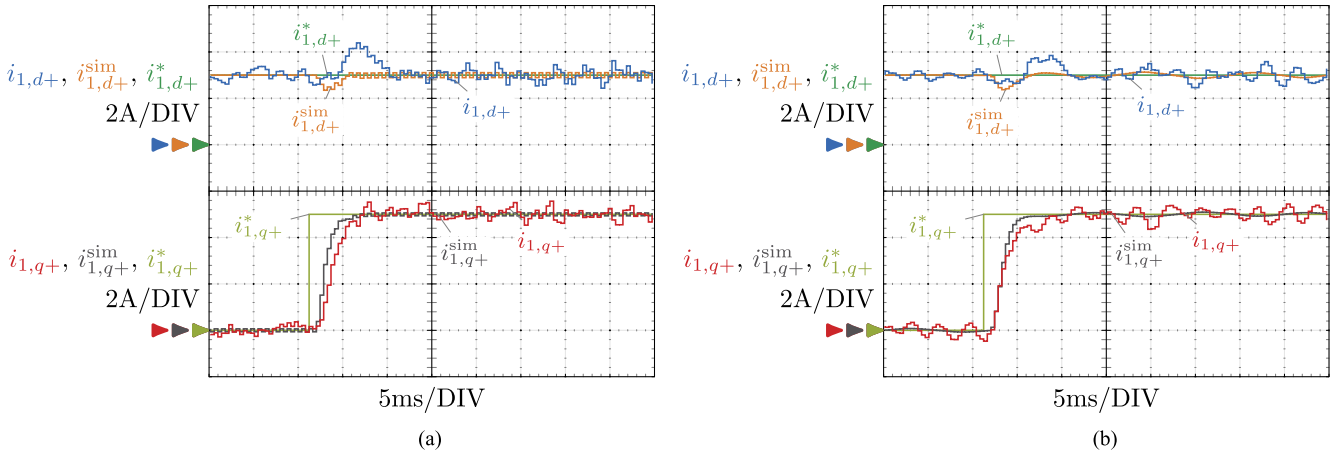

Fig. 9. Experimental and simulation waveforms ($i_{1,\text{dq}}$ and $i^{\text{sim}}_{1,\text{dq}}$, respectively) for a reference step $i^{*}_{1,q+}$ in the positive synchronous frame dq+ rotating at the fundamental grid frequency ω_g. (a) *LCL* filter I and (b) *LCL* filter II.

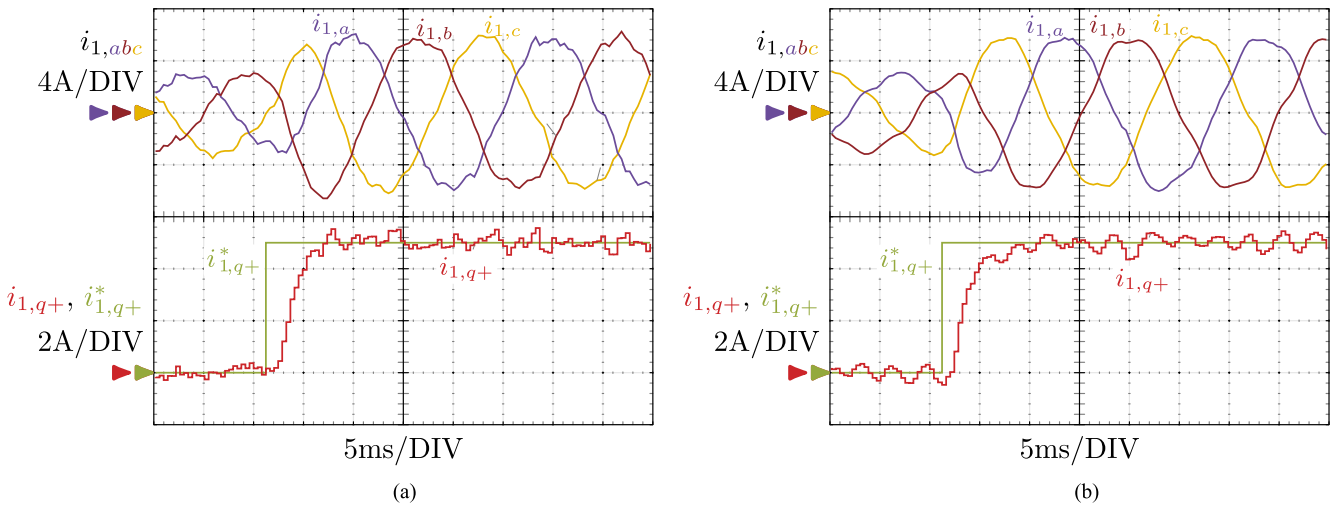

Fig. 10. Experimental phase currents ($i_{1,\text{abc}}$) for a reference step $i^{*}_{1,q+}$ in the imaginary component ($i_{1,q+}$) of the positive synchronous frame dq+ rotating at the fundamental grid frequency ω_g. (a) *LCL* filter I and (b) *LCL* filter II.

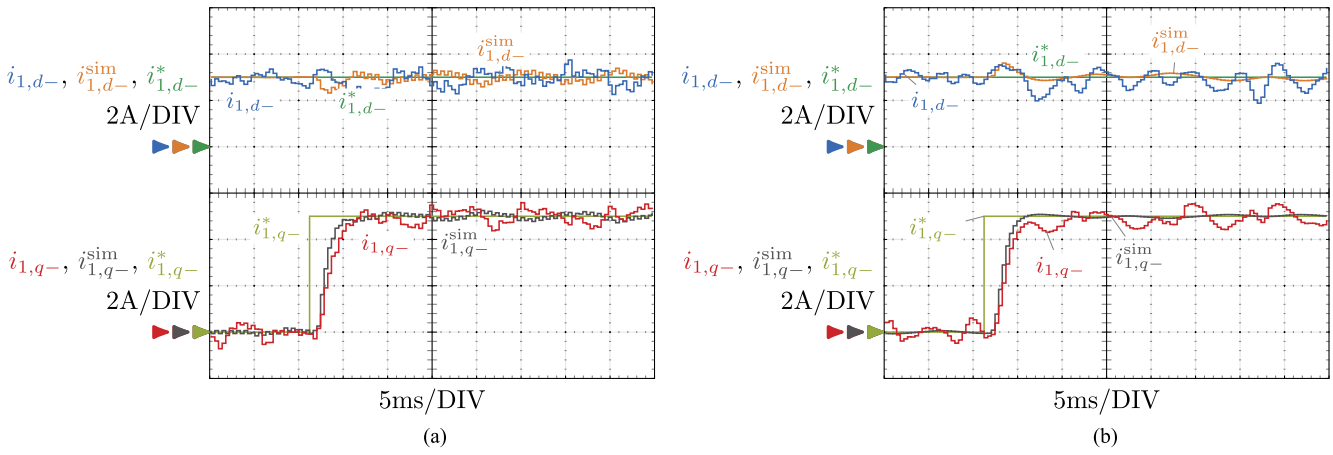

Fig. 11. Experimental and simulation waveforms ($i_{1,\text{dq}}$ and $i^{\text{sim}}_{1,\text{dq}}$, respectively) for a reference step $i^{*}_{1,q-}$ in the negative synchronous frame dq− rotating at the fundamental grid frequency ω_g. (a) *LCL* filter I and (b) *LCL* filter II.

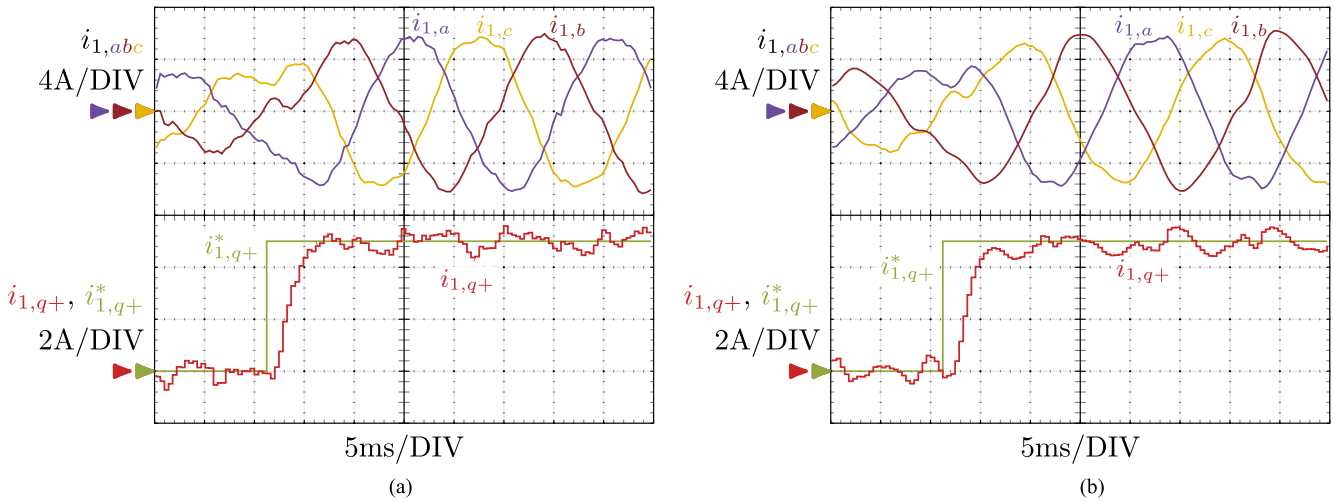

Fig. 12. Experimental phase currents ($i_{1,\mathrm{abc}}$) for a reference step $i^*_{1,q-}$ in the imaginary component ($i_{1,q-}$) of the negative synchronous frame dq− rotating at the fundamental grid frequency ω_g. (a) *LCL* filter I and (b) *LCL* filter II.

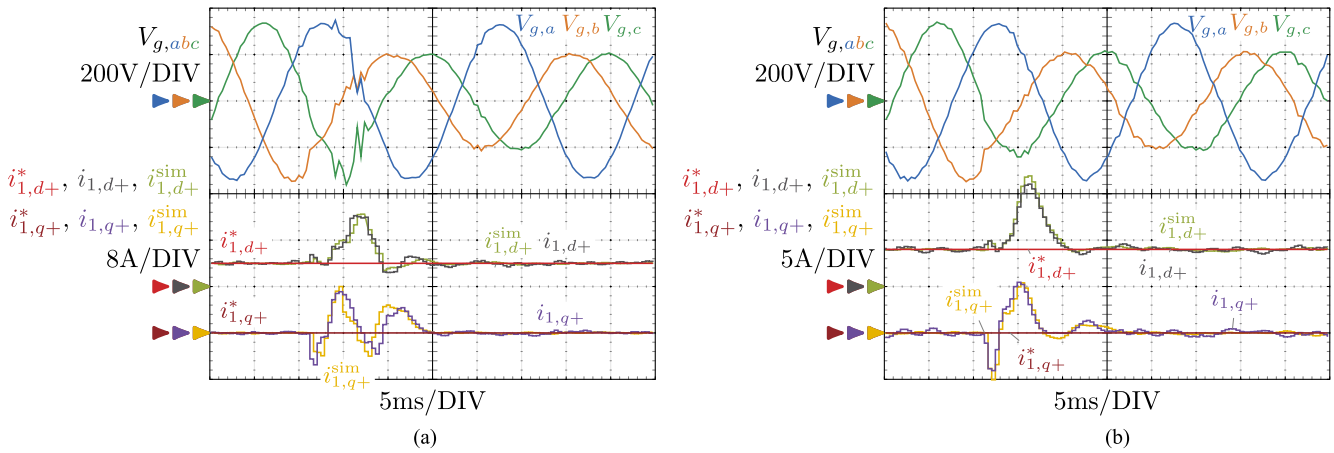

Fig. 13. Experimental and simulation waveforms ($i_{1,\mathrm{dq}}$ and $i^{\mathrm{sim}}_{1,\mathrm{dq}}$, respectively) for a 40%-depth type-C sag $V_{g,\mathrm{abc}}$ [43] while keeping the reference $i^*_{1,\mathrm{dq}}$ constant. (a) *LCL* filter I and (b) *LCL* filter II.

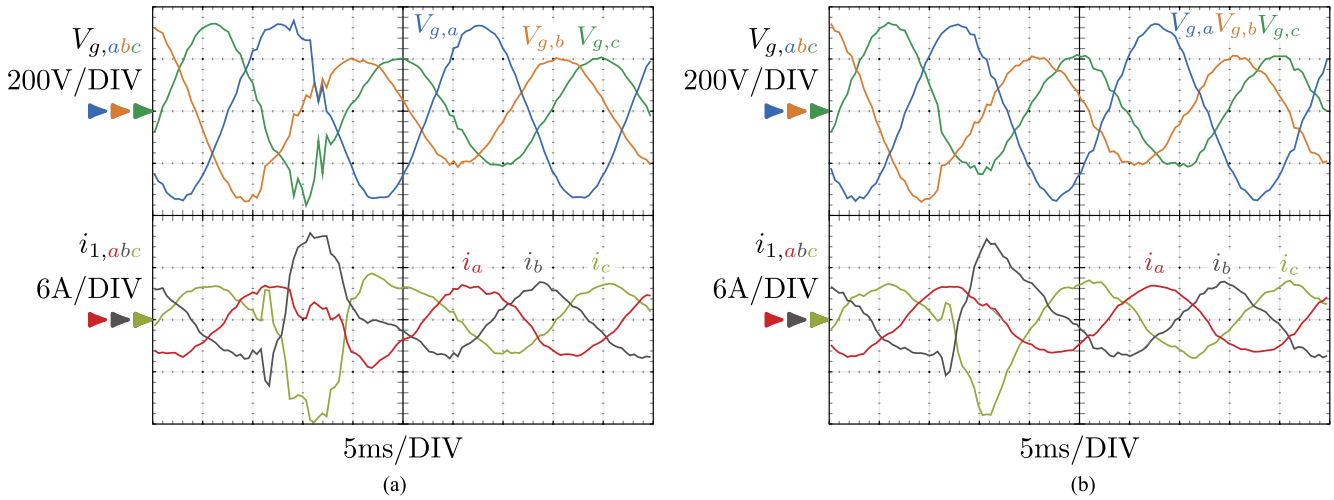

Fig. 14. Experimental phase currents ($i_{1,\mathrm{abc}}$) for a 40%-depth type-C sag $V_{g,\mathrm{abc}}$ [43] while keeping the reference constant. (a) *LCL* filter I and (b) *LCL* filter II.

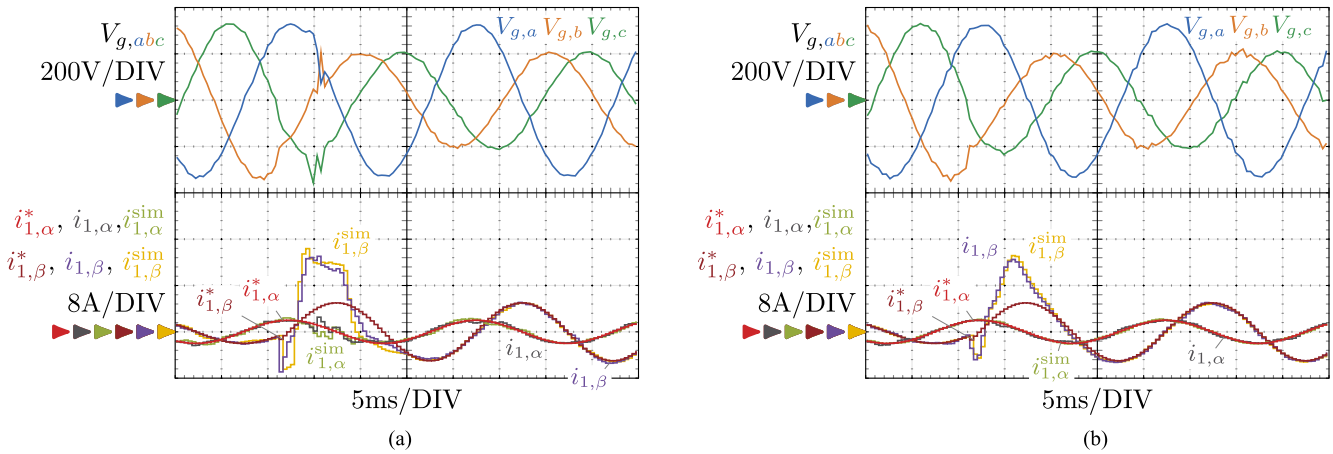

Fig. 15. Experimental and simulation waveforms (i_1 and $i_1^{\rm sim}$, respectively) for a 40%-depth type-C sag $V_{g,\rm abc}$ [43]. The reference step i_1^* is calculated according to the so-called positive-negative-sequence compensation strategy [45]. (a) *LCL* filter I and (b) *LCL* filter II.

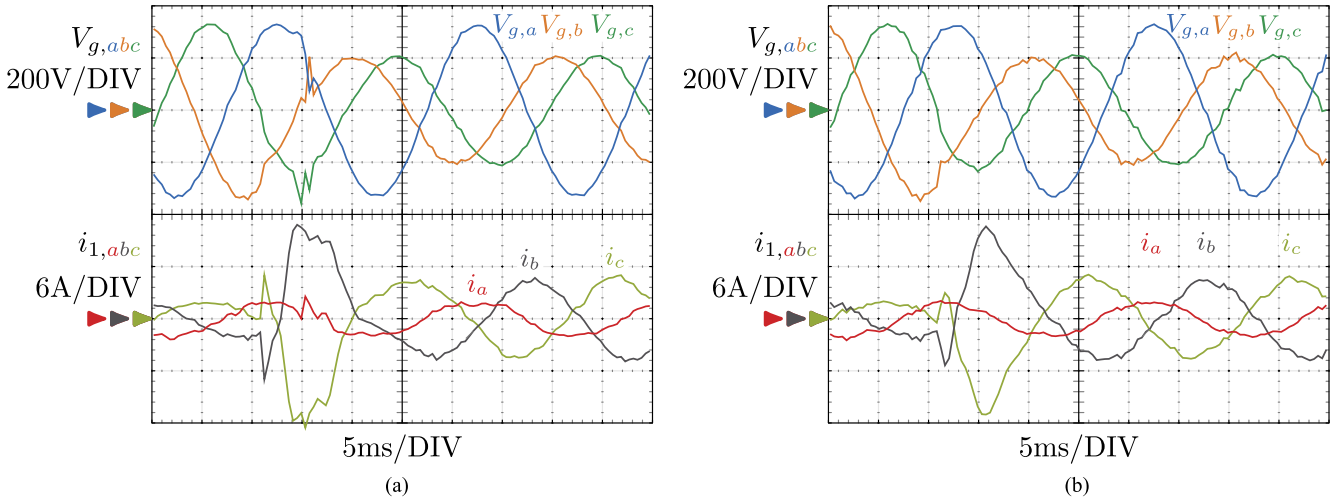

Fig. 16. Experimental phase currents ($i_{1,\rm abc}$) for a 40%-depth type-C sag $V_{g,\rm abc}$ [43]. The reference step i_1^* is calculated according to the so-called positive-negative-sequence compensation strategy [45]. (a) *LCL* filter I and (b) *LCL* filter II.

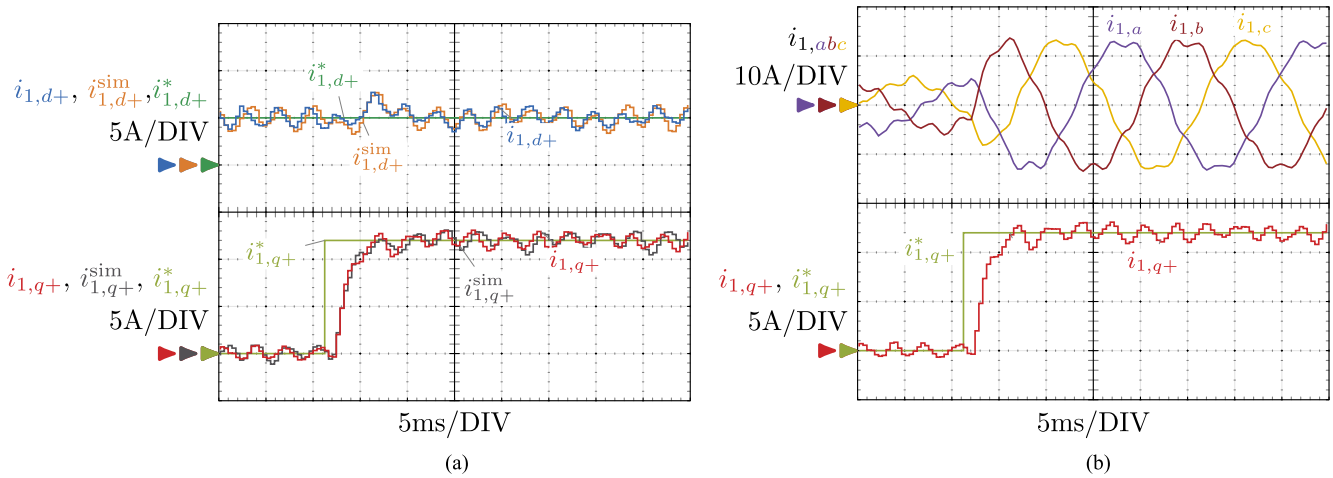

Fig. 17. Waveforms for a reference step $i^*_{1,q+}$ in the positive synchronous frame dq+. The grid voltage has the following low-order voltage harmonics: $V_3 = 1.2$ V, $V_5 = 0.7$ V, $V_7 = 4.8$ V, and $V_9 = 1.6$ V. *LCL* filter I is used for the test. (a) Experimental and simulation synchronous-frame waveforms ($i_{1,\rm dq+}$ and $i^{\rm sim}_{1,\rm dq+}$, respectively). (b) Experimental phase currents $i_{1,\rm abc}$.

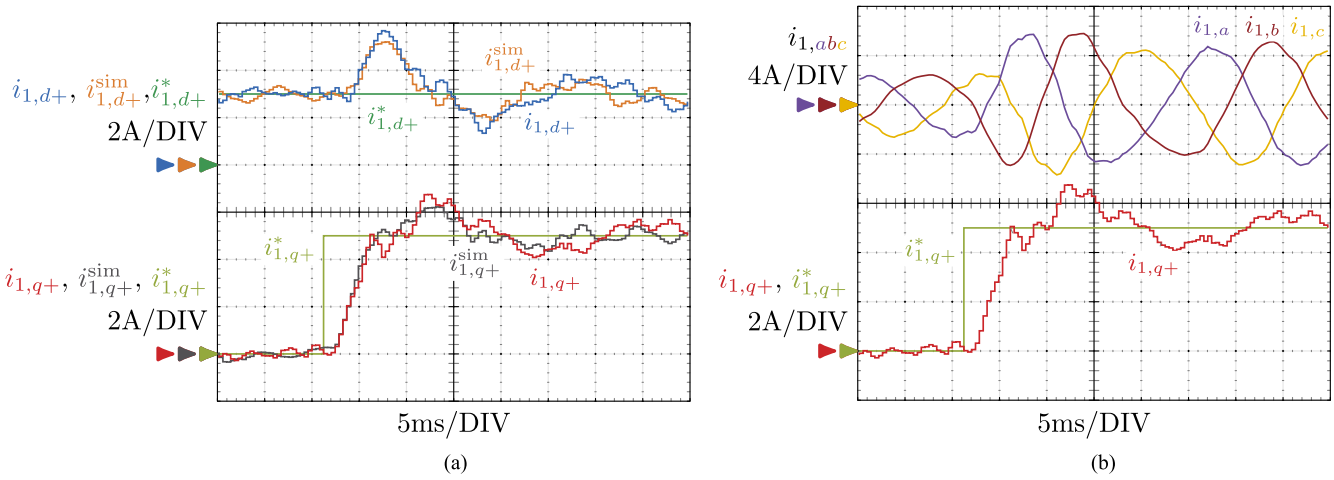

Fig. 18. Waveforms for a reference step $i^{*}_{1,q+}$ in the positive synchronous frame dq+. The filter inductances, L_1 and L_2, are 2.8 times bigger than their nominal values (those of filter II). (a) Experimental and simulation synchronous-frame waveforms ($i_{1,\text{dq+}}$ and $i^{\text{sim}}_{1,\text{dq+}}$, respectively). (b) Experimental phase currents $i_{1,\text{abc}}$.

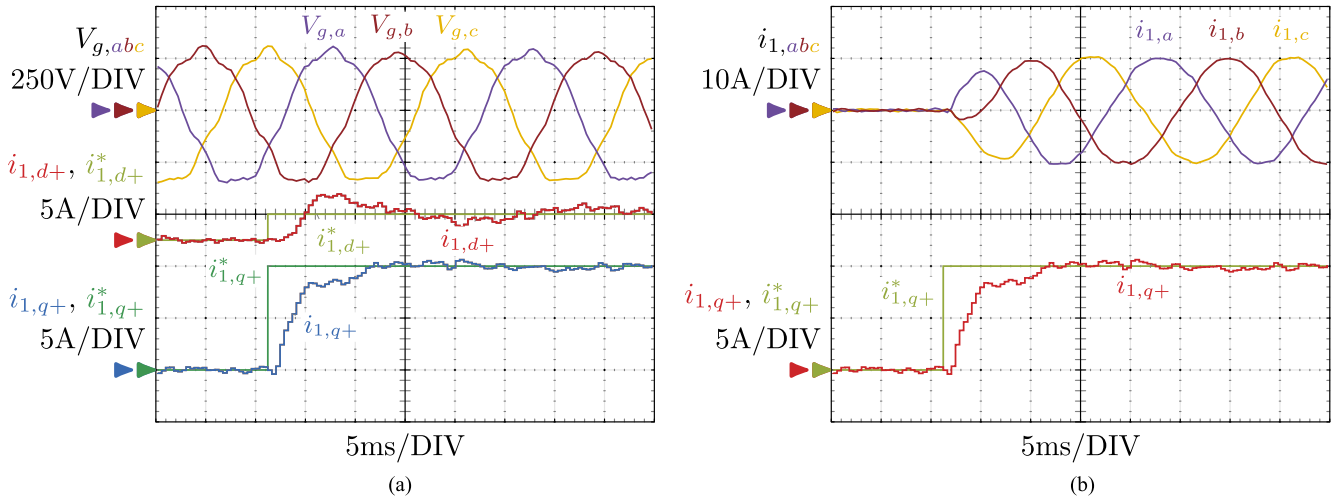

Fig. 19. Waveforms for a reference step $i^{*}_{1,\text{dq+}}$ in the positive synchronous frame dq+ rotating at the fundamental grid frequency, using the *LCL* filter I and connected to a weak grid $V_{g,\text{abc}}$ with a grid impedance $Z_g = 0.11$ p.u. (a) Experimental synchronous-frame currents $i_{1,\text{dq+}}$. (b) Experimental phase currents $i_{1,\text{abc}}$.

$V_5 = 0.3\%$, $V_7 = 2.1\%$, and $V_9 = 0.7\%$, where the subscript denotes the harmonic order. The PLL [44] includes a moving average filter, which eliminates their effect on the phase estimation. The fifth and seventh voltage harmonics cause the 500-mA sixth-harmonic current that can be seen in the dq frame. The harmonic current is low because of the good robustness of the controller to the grid voltage harmonics. Fig. 18 shows the robustness of the control to variations in the plant parameters. In order to do this, a design is made according to the filter I parameters, but the real plant in the setup has the inductances of filter II (L_1 and L_2 are 2.8 times bigger than their nominal values). The response exhibits a certain overshoot and axis cross-coupling because of the closed-loop poles displaced due to this discrepancy. Nevertheless, the system is stable despite the large parameter variations.

In Fig. 19, the VSC is connected to the weak grid presented in Section IV. In this case, the dynamics of the PLL are coupled to the dynamics of the current controller [46], [47]. Nevertheless, no significant variations in the transient response parameters are observed.

VI. Conclusion

This paper has presented a current controller of both positive and negative grid-side current sequences for grid-tied converters with *LCL* filter. The proposed controller offers fast reference-tracking capability with negligible overshoot and low controller effort, regardless of the switching frequency and *LCL* filter used: f_{res} above or below $f_s/6$. The controller has also been proved to be robust to disturbances, such as voltage sags and low-order voltage harmonics, even when combined with reference

changes in both sequences. The sensitivity to parameter variations was analyzed obtaining a low sensitivity. The developed method (based on direct discrete-time pole placement) provides a simple process for the design of the controller, and includes estimated losses of the plant in the model. This method makes it possible to design a controller for any plant based on an *LCL* filter so that a stable operation is ensured, without additional damping methods. The design was verified using simulations and experiments.

APPENDIX
OBSERVER FORMULAS

A state-feedback control needs to reconstruct the system state variables. This appendix derives the equation that the reduced-order estimator implements to calculate the unmeasured state variables. The estimator uses the model of the observed system (9). To obtain an estimator for only the unmeasured part of the state vector, a partition of the state vector $\mathbf{x}(k)$ is defined: $x_a(k) = i_1(k)$ is the measured part, which is the grid-side current; and $\mathbf{x_b}(k) = [i_2 \;\; v \;\; u_d \;\; r_1 \;\; r_2]^{\mathrm{T}}$ includes the rest of the state variables to be estimated. Therefore, the resultant system description, from (9), becomes

$$\underbrace{\begin{bmatrix} x_a(k+1) \\ \mathbf{x_b}(k+1) \end{bmatrix}}_{\mathbf{x_3}(k+1)} = \underbrace{\begin{bmatrix} F_{\mathrm{aa}} & \mathbf{F_{ab}} \\ \mathbf{F_{ba}} & \mathbf{F_{bb}} \end{bmatrix}}_{\mathbf{F_3}} \underbrace{\begin{bmatrix} x_a(k) \\ \mathbf{x_b}(k) \end{bmatrix}}_{\mathbf{x_3}(k)} + \underbrace{\begin{bmatrix} G_a \\ \mathbf{G_b} \end{bmatrix}}_{\mathbf{G_3}} u(k)$$

$$i_1(k) = \begin{bmatrix} 1 & \mathbf{0} \end{bmatrix} \begin{bmatrix} x_a(k+1) \\ \mathbf{x_b}(k+1) \end{bmatrix}. \tag{12}$$

Then, the observer gain $\mathbf{K_o}$ for the reduced-order estimator is calculated so as to have the observer closed-loop poles at the desired positions. This can be done by solving Ackermann's estimator formula [36] by executing one of the following two MaTLAB commands: $\mathbf{K_o} = \mathtt{place}(\mathbf{F_{bb}}^{\mathrm{T}}, \mathbf{F_{ab}}^{\mathrm{T}}, \mathbf{p})$ or $\mathbf{K_o} = \mathtt{acker}(\mathbf{F_{bb}}^{\mathrm{T}}, \mathbf{F_{ab}}^{\mathrm{T}}, \mathbf{p})$, where $\mathbf{p}$ is a vector with the desired poles.

Notice that the current state estimation $\hat{\mathbf{x}}_\mathbf{b}(k)$ of (10) depends on the last measurement available $i_1(k)$. Moreover, the dynamics of the observer are determined by $\mathbf{F_{bb}} - \mathbf{K_o F_{ab}}$, which has one eigenvalue (pole) less than the system matrix $\mathbf{F_3}$.

Finally, the feedforward gain K_f is computed as $K_f = N_u + \mathbf{K_c N_x}$ [36], where

$$\begin{bmatrix} \mathbf{N_x} \\ N_u \end{bmatrix} = \begin{bmatrix} \mathbf{F_2} - \mathbf{I} & \mathbf{G_2} \\ \mathbf{H_2} & 0 \end{bmatrix}^{-1} \begin{bmatrix} \mathbf{0} \\ 1 \end{bmatrix}. \tag{13}$$

REFERENCES

[1] B. K. Bose, "Global energy scenario and impact of power electronics in 21st century," *IEEE Trans. Ind. Electron.*, vol. 60, no. 7, pp. 2638–2651, Jul. 2013.

[2] P. Channegowda and V. John, "Filter optimization for grid interactive voltage source inverters," *IEEE Trans. Ind. Electron.*, vol. 57, no. 12, pp. 4106–4114, Dec. 2010.

[3] G. Shen, X. Zhu, J. Zhang, and D. Xu, "A new feedback method for PR current control of LCL-filter-based grid-connected inverter," *IEEE Trans. Ind. Electron.*, vol. 57, no. 6, pp. 2033–2041, Jun. 2010.

[4] M. Liserre, F. Blaabjerg, and S. Hansen, "Design and control of an LCL-filter-based three-phase active rectifier," *IEEE Trans. Ind. Appl.*, vol. 41, no. 5, pp. 1281–1291, Sep./Oct. 2005.

[5] A. G. Yepes, A. Vidal, O. López, and J. Doval-Gandoy, "Evaluation of techniques for cross-coupling decoupling between orthogonal axes in double synchronous reference frame current control," *IEEE Trans. Ind. Electron.*, vol. 61, no. 7, pp. 3527–3531, Jul. 2014.

[6] B. Li, W. Yao, L. Hang, and L. M. Tolbert, "Robust proportional resonant regulator for grid-connected voltage source inverter (VSI) using direct pole placement design method," *IET Power Electron.*, vol. 5, no. 8, pp. 1367–1373, Sep. 2012.

[7] A. Vidal, A. G. Yepes, F. D. Freijedo, J. Malvar, O. López, and J. Doval-Gandoy, "A technique to estimate the equivalent loss resistance of grid-tied converters for current control analysis and design," *IEEE Trans. Power Electron.*, vol. 30, no. 3, pp. 1747–1761, Mar. 2015.

[8] S. G. Parker, B. P. McGrath, and D. G. Holmes, "Regions of active damping control for LCL filters," *IEEE Trans. Ind. Appl.*, vol. 50, no. 1, pp. 424–432, Jan./Feb. 2014.

[9] C. A. Busada, S. Gomez Jorge, and J. A. Solsona, "Full-state feedback equivalent controller for active damping in LCL-filtered grid-connected inverters using a reduced number of sensors," *IEEE Trans. Ind. Electron.*, vol. 62, no. 10, pp. 5993–6002, Oct. 2015.

[10] R. Peña-Alzola, M. Liserre, F. Blaabjerg, R. Sebastián, J. Dannehl, and F. W. Fuchs, "Analysis of the passive damping losses in LCL-filter-based grid converters," *IEEE Trans. Power Electron.*, vol. 28, no. 6, pp. 2642–2646, Jun. 2013.

[11] Y. Jia, J. Zhao, and X. Fu, "Direct grid current control of LCL-filtered grid-connected inverter mitigating grid voltage disturbance," *IEEE Trans. Power Electron.*, vol. 29, no. 3, pp. 1532–1541, Mar. 2014.

[12] D. Pan, X. Ruan, C. Bao, W. Li, and X. Wang, "Optimized controller design for LCL-type grid-connected inverter to achieve high robustness against grid-impedance variation," *IEEE Trans. Ind. Electron.*, vol. 62, no. 3, pp. 1537–1547, Mar. 2015.

[13] Y. Tang, P. C. Loh, P. Wang, F. H. Choo, F. Gao, and F. Blaabjerg, "Generalized design of high performance shunt active power filter with output LCL filter," *IEEE Trans. Ind. Electron.*, vol. 59, no. 3, pp. 1443–1452, Mar. 2012.

[14] J. Dannehl, F. W. Fuchs, S. Hansen, and P. B. Thogersen, "Investigation of active damping approaches for PI-based current control of grid-connected pulse width modulation converters with LCL filters," *IEEE Trans. Ind. Appl.*, vol. 46, no. 4, pp. 1509–1517, Jul./Aug. 2010.

[15] L. Harnefors, A. G. Yepes, A. Vidal, and J. Doval-Gandoy, "Passivity-based controller design of grid-connected VSCs for prevention of electrical resonance instability," *IEEE Trans. Ind. Electron.*, vol. 62, no. 2, pp. 702–710, Jan./Feb. 2015.

[16] C. Citro, P. Siano, and C. Cecati, "Designing inverters' current controllers with resonance frequencies cancellation," *IEEE Trans. Ind. Electron.*, vol. 63, no. 5, pp. 3072–3080, May 2016.

[17] R. Peña-Alzola, M. Liserre, F. Blaabjerg, R. Sebastián, J. Dannehl, and F. W. Fuchs, "Systematic design of the lead-lag network method for active damping in LCL-filter based three phase converters," *IEEE Trans. Ind. Informat.*, vol. 10, no. 1, pp. 43–52, Feb. 2014.

[18] H. Komurcugil, N. Altin, S. Ozdemir, and I. Sefa, "Lyapunov-function and proportional-resonant-based control strategy for single-phase grid-connected VSI with LCL filter," *IEEE Trans. Ind. Electron.*, vol. 63, no. 5, pp. 2838–2849, May 2016.

[19] X. Wang, F. Blaabjerg, and P. C. Loh, "Grid-current-feedback active damping for LCL resonance in grid-connected voltage-source converters," *IEEE Trans. Power Electron.*, vol. 31, no. 1, pp. 213–223, Jan. 2016.

[20] M. Hanif, V. Khadkikar, W. Xiao, and J. L. Kirtley, "Two degrees of freedom active damping technique for LCL filter-based grid connected PV systems," *IEEE Trans. Ind. Electron.*, vol. 61, no. 6, pp. 2795–2803, Jun. 2014.

[21] J. Xu, S. Xie, and T. Tang, "Active damping-based control for grid-connected LCL-filtered inverter with injected grid current feedback only," *IEEE Trans. Ind. Electron.*, vol. 61, no. 9, pp. 4746–4758, Sep. 2014.

[22] E. Wu and P. W. Lehn, "Digital current control of a voltage source converter with active damping of LCL resonance," *IEEE Trans. Power Electron.*, vol. 21, no. 5, pp. 1364–1373, Sep. 2006.

[23] B. Bahrani, M. Vasiladiotis, and A. Rufer, "High-order vector control of grid-connected voltage-source converters with LCL-filters," *IEEE Trans. Ind. Electron.*, vol. 61, no. 6, pp. 2767–2775, Jun. 2014.

[24] R. Meyer, A. Zlotnik, and A. Mertens, "Fault ride-through control of medium-voltage converters with LCL filter in distributed generation systems," *IEEE Trans. Ind. Appl.*, vol. 50, no. 5, pp. 3448–3456, Sep./Oct. 2014.
[25] N. Panten, N. Hoffmann, and F. W. Fuchs, "Finite control set model predictive current control for grid-connected voltage-source converters with LCL filters: A study based on different state feedbacks," *IEEE Trans. Power Electron.*, vol. 31, no. 7, pp. 5189–5200, Jul. 2016.
[26] K. Nishida, T. Ahmed, and M. Nakaoka, "A novel finite-time settling control algorithm designed for grid-connected three-phase inverter with an LCL-type filter," *IEEE Trans. Ind. Appl.*, vol. 50, no. 3, pp. 2005–2020, May/Jun. 2014.
[27] Y. A. R. I. Mohamed, M. A. Rahman, and R. Seethapathy, "Robust line-voltage sensorless control and synchronization of LCL-filtered distributed generation inverters for high power quality grid connection," *IEEE Trans. Power Electron.*, vol. 27, no. 1, pp. 87–98, Jan. 2012.
[28] J. R. Massing, M. Stefanello, H. A. Grundling, and H. Pinheiro, "Adaptive current control for grid-connected converters with LCL filter," *IEEE Trans. Ind. Electron.*, vol. 59, no. 12, pp. 4681–4693, Dec. 2012.
[29] I. J. Gabe, V. F. Montagner, and H. Pinheiro, "Design and implementation of a robust current controller for VSI connected to the grid through an LCL filter," *IEEE Trans. Power Electron.*, vol. 24, no. 6, pp. 1444–1452, Jun. 2009.
[30] M. Xue, Y. Zhang, Y. Kang, Y. Yi, S. Li, and F. Liu, "Full feedforward of grid voltage for discrete state feedback controlled grid-connected inverter with LCL filter," *IEEE Trans. Power Electron.*, vol. 27, no. 10, pp. 4234–4247, Oct. 2012.
[31] J. Kukkola and M. Hinkkanen, "Observer-based state-space current control for a three-phase grid-connected converter equipped with an LCL filter," *IEEE Trans. Ind. Appl.*, vol. 50, no. 4, pp. 2700–2709, Jul./Aug. 2014.
[32] J. Kukkola, M. Hinkkanen, and K. Zenger, "Observer-based state-space current controller for a grid converter equipped with an LCL filter: Analytical method for direct discrete-time design," *IEEE Trans. Ind. Appl.*, vol. 51, no. 5, pp. 4079–4090, Sep./Oct. 2015.
[33] J. Dannehl, F. W. Fuchs, and P. B. Thogersen, "PI state space current control of grid-connected PWM converters with LCL filters," *IEEE Trans. Power Electron.*, vol. 25, no. 9, pp. 2320–2330, Sep. 2010.
[34] C. Ramos, A. Martins, and A. Carvalho, "Complex state-space current controller for grid-connected converters with an LCL filter," in *Proc. 35th Annu. Conf. IEEE Ind. Electron.*, Nov. 2009, pp. 296–301.
[35] L. A. Maccari *et al.* "LMI-based control for grid-connected converters with LCL filters under uncertain parameters," *IEEE Trans. Power Electron.*, vol. 29, no. 7, pp. 3776–3785, Jul. 2014.
[36] G. F. Franklin, J. D. Powell, and M. L. Workman, *Digital Control of Dynamic Systems*, 3rd ed. Reading, MA, USA: Addison-Wesley, 1998, pp. 202–203, 110, 322–336, 308–309, 400–403, 289–301, 286.
[37] S. Buso and P. Mattavelli, *Digital Control in Power Electronics*. Ed. Morgan and Claypool Publishers, 2006.
[38] D. Maksimovic and R. Zane, "Small-signal discrete-time modeling of digitally controlled PWM converters," *IEEE Trans. Power Electron.*, vol. 22, no. 6, pp. 2552–2556, Nov. 2007.
[39] D. M. V. de Sype, K. D. Gusseme, F. M. L. L. D. Belie, A. P. V. den Bossche, and J. A. Melkebeek, "Small-signal z-domain analysis of digitally controlled converters," *IEEE Trans. Power Electron.*, vol. 21, no. 2, pp. 470–478, Mar. 2006.
[40] X. Zhang, J. W. Spencer, and J. M. Guerrero, "Small-signal modeling of digitally controlled grid-connected inverters with LCL filters," *IEEE Trans. Ind. Electron.*, vol. 60, no. 9, pp. 3752–3765, Sep. 2013.
[41] G. C. Goodwin, S. F. Graebe, and M. E. Salgado, *Control System Design*. 1st ed., Prentice Hall, 2001, p. 355.
[42] Y. W. Li and C. N. Kao, "An accurate power control strategy for power-electronics-interfaced distributed generation units operating in a low-voltage multibus microgrid," *IEEE Trans. Power Electron.*, vol. 24, no. 12, pp. 2977–2988, Dec. 2009.
[43] M. H. Bollen, *Understanding Power Quality Problems: Voltage Sags and Interruptions*. 1st ed., New York: Wiley, 1999, p. 194.
[44] F. D. Freijedo, J. Doval-Gandoy, O. López, and E. Acha, "Tuning of phase-locked loops for power converters under distorted utility conditions," *IEEE Trans. Ind. Appl.*, vol. 45, no. 6, pp. 2039–2047, Nov./Dec. 2009.
[45] P. Rodriguez, A. V. Timbus, R. Teodorescu, M. Liserre, and F. Blaabjerg, "Flexible active power control of distributed power generation systems during grid faults," *IEEE Trans. Ind. Electron.*, vol. 54, no. 5, pp. 2583–2592, Oct. 2007.
[46] Y. A.-R. I. Mohamed and M. Davari, "Dynamics and robust vector control of a very weak grid-connected voltage-source converter considering the phase locked loop dynamics," *IEEE Trans. Power Electron.*, accepted for publication.
[47] D. Dong, B. Wen, D. Boroyevich, P. Mattavelli, and Y. Xue, "Analysis of phase-locked loop low-frequency stability in three-phase grid-connected power converters considering impedance interactions," *IEEE Trans. Ind. Electron.*, vol. 62, no. 1, pp. 310–321, Jan. 2015.

Diego Pérez-Estévez (S'15) received the M.Sc. degree, in 2014, from the University of Vigo, Vigo, Spain, where he is currently working toward the Ph.D. degree in the Applied Power Electronics Technology Research Group.

Since 2014, he has been with the Applied Power Electronics Technology Research Group. His research interests include control of grid-connected converters and distributed power generation systems.

Jesús Doval-Gandoy (M'99) received the M.Sc. degree in electrical engineering from the Polytechnic University of Madrid, in 1991, and the Ph.D. degree in electrical engineering from the University of Vigo, in 1999.

From 1991 till 1994, he worked at industry. He is currently the head of the Applied Power Electronics Technology Research Group, University of Vigo. His research interests are in the areas of ac power conversion.

Alejandro G. Yepes (S'10–M'12) received the M.Sc. and Ph.D. degrees from the University of Vigo, Vigo, Spain, in 2009 and 2011, respectively.

Since 2008, he has been with the Applied Power Electronics Technology Research Group, University of Vigo. His main research interests include control of switching power converters and ac drives.

Óscar López (M'05–SM'16) received the M.Sc. and Ph.D. degrees from the University of Vigo, Vigo, Spain, in 2001 and 2009, respectively.

Since 2004, he has been an Assistant Professor at the University of Vigo. He is a member of the Applied Power Electronics Technology Research Group, University of Vigo. His research interests include the areas of ac power switching converters technology.